The Transition between Reactive and Radiative Regimes for Leaky Modes in Planar Waveguides based on Homogenized Partially Reflecting Surfaces

Walter Fuscaldo, *Member, IEEE,* Paolo Burghignoli, *Senior Member, IEEE,* and Alessandro Galli, *Member, IEEE*

***Abstract*—The gradual transition from a reactive to a radiative regime is studied for leaky modes supported by multilayered planar open waveguides. The so-called *leaky cutoff* condition, i.e., the frequency for which the leaky phase constant β equals the leaky attenuation constant α, originally introduced for microstrip lines and other printed structures, is investigated here with the aim of providing detailed information on the relative amount of reactive and radiative attenuation for leaky modes excited by finite sources and propagating as cylindrical waves along general planar waveguides. Analytical results are derived on the basis of a lossy parallel-plate-waveguide model and are validated through full-wave numerical simulations of two-dimensional leaky-wave structures based on grounded slabs covered with lossless or lossy partially reflecting surfaces (including, e.g., graphene layers) that can be treated as homogenized sheets. An analysis of the complex wave impedance of the considered leaky modes is also provided, in order to assess the frequency ranges where a good input matching can be expected for practical sources. In this regard, an ad hoc impedance matching network is designed and full-wave validated for a specific case to show that is indeed possible to achieve a good impedance matching below cutoff in practical designs.**

***Index Terms*—Electromagnetic analysis, Fabry–Perot cavities, frequency selective surfaces, graphene, leaky waves, planar waveguides, terahertz radiation.**

I. Introduction

LEAKY modes of open electromagnetic waveguides have constituted an intriguing subject since their discovery in the 1930s and the first theoretical assessments in the 1950s [1], thanks both to their unusual, often counter-intuitive mathematical and physical properties and to their effectiveness in modeling otherwise complicated radiative phenomena, associated with partially guided propagation (see, e.g., [2]–[4] and references therein).

Leaky modes have a complex wavenumber (say, $k_z = \beta - j\alpha$) also in lossless open waveguides, since the imaginary part of the wavenumber takes into account both radiation losses and reactive effects (in addition to material losses, if present). Furthermore, they often have an *improper* nature, i.e., their modal field exponentially grows at infinity in the transverse direction (we recall that *forward*, i.e., $\beta > 0$ leaky modes retain an *improper* nature, whereas *backward*, i.e., $\beta < 0$ leaky modes retain a *proper* nature [3]). These features do not allow for applying to leaky modes many standard definitions and concepts applicable to bound modes supported by open or closed waveguides. Referring to, for instance, planar printed waveguides, such as striplines, microstrip lines, slotlines, etc., non-standard definitions have been introduced in order to extend to leaky regimes such familiar concepts as the characteristic impedance [5], [6] or the scattering matrix [7].

This paper is an expanded version from the International Microwave Symposium 2020, Los Angeles, CA, 21–26 Jun. 2020.

W. Fuscaldo, P. Burghignoli, and A. Galli are with the Department of Information Engineering, Electronics and Telecommunications, Sapienza University of Rome, 00184 Rome, Italy e-mail: {walter.fuscaldo/paolo.burghignoli/alessandro.galli}@uniroma1.it

Manuscript received Xxxx yyyy, zzzz; revised Xxxx yyyy, zzzz.

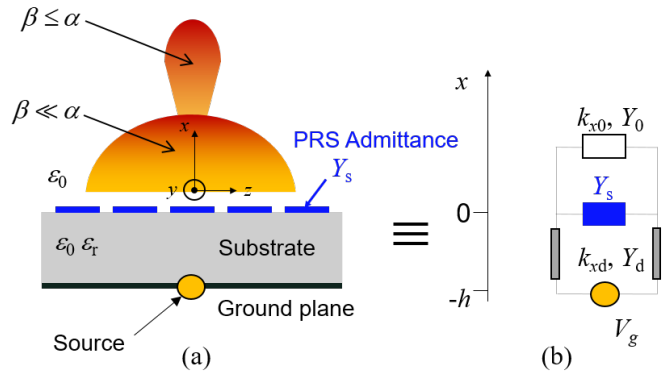

Fig. 1. (a) The evolution of the radiation pattern of a planar waveguide based on a PRS, namely an FPC-LWA, below the leaky cutoff $\beta = \alpha$. As the frequency increases approaching the leaky cutoff, the power density at broadside increases; this behavior can be interpreted as a consequence of the transition from the reactive regime to the radiative regime. (b) Relevant transverse equivalent network.

Indeed, the very basic concept of modal cutoff needs a special consideration for a leaky mode. Among the few studies on this aspect, in [8] the condition of leaky cutoff $\beta = \alpha$ was first introduced for the fundamental leaky mode of a microstrip line, as the boundary between a low-frequency, reactive regime (where $\beta < \alpha$) and a high-frequency, radiative regime (where $\beta > \alpha$). The same condition was also derived in [9] by means of a simple effective-dielectric-constant approach, and has been applied over the years to a number of cases, such as microstrips operated on higher leaky modes [10], circular dielectric rods and waveguides [11], [12], Goubau lines [13], modified microstrip lines [14], etc.

Planar waveguides based on partially reflecting surfaces (PRSs) (i.e., parallel-plate waveguides (PPWs) where the upper plate is replaced with a PRS) also support leaky modes. When excited by finite sources in the center, these modes propagate along the structure cylindrical leaky waves and may

produce useful radiative effects exploited, e.g., in Fabry–Perot cavity leaky-wave antennas (FPC-LWAs) [3]. We note here that with the term 'FPC-LWAs' we only refer to LWAs based on homogenized PRS, i.e, uniform or quasi-uniform LWAs that support the propagation of forward leaky modes only.

It is well known that, in the infinite aperture case [15] (the finite case being analyzed in [16], [17]), cylindrical leaky waves radiate a broadside beam as long as $\beta \leq \alpha$ (see Fig. 1). Therefore, the *leaky cutoff condition* $\beta = \alpha$ is also called in this context *beam-splitting condition*. When $\beta = \alpha$, the radiated power density at broadside is maximized, hence most of the studies on FPC-LWAs optimize and analyze the structure to work at the leaky cutoff frequency, or above.

We should stress here that these radiating features only apply to uniform or quasi-uniform LWAs, i.e., based on homogenized PRS, and excited by 1-D bidirectional or 2-D cylindrical leaky waves. Conversely, periodic LWAs (either provided with 1-D unidirectional or 2-D cylindrical excitation) designed to have the $n = -1$ space harmonic in the radiating regime, generally support backward and forward leaky waves: thus, a broadside beam is only radiated for $|\beta| \leq \alpha$ provided the open stopband is suitably suppressed [3], whereas for $|\beta| > \alpha$ a dual-beam or a conical beam is created depending on the source type (although for truncated structures a broadside beam can exist also for $|\beta|$ somewhat larger than α [16], [17]).

It is also known, however, that the beamwidth of FPC-LWAs is minimized (and in turn the directivity is maximized) when $\beta \simeq 0.5176\alpha$ [15], [17], thus motivating the interest in designing FPC-LWAs working below the leaky cutoff. To the Authors' best knowledge, in the current literature, a clear and general analysis of the transition region between the reactive and the radiative behavior of cylindrical leaky waves below cutoff, also including the effect of material losses, is still lacking and is the object of the present analysis.

To this aim, we start by considering in Section II, the simplest case of guided modes in *lossy* PPWs. The *equivalent* loss tangent models here *any* kind of losses [15], [18]. Comparison between the modes in *lossy* and *lossless* PPWs allows for determining the transition between *reactive* attenuation and *all* other kinds of losses. We here define useful figures of merit and derive significant analytical results.

In Section III, we examine the relevant case of planar waveguides based on PRS, highlighting their connection to *lossy* PPWs through a suitable definition of the equivalent loss tangent [18]. The analytical results are here compared with independent numerical simulations for several cases of interest to show the accuracy and the range of validity of the proposed analysis. An application to the analysis of graphene planar waveguides (GPWs) operating in the THz range is also presented to test the method for cases that lie beyond the range of validity of the previous expressions. The performance of the proposed antenna is validated through full-wave simulations confirming that an FPC-LWA based on a homogenized PRS reaches maximum directivity at broadside below the cutoff frequency. For this specific case, an ad hoc impedance matching network is designed to show that it is possible to achieve a good realized gain even below the cutoff frequency.

In Section IV, the wave impedance is also analyzed, and more general considerations about potential impedance matching issues at frequencies below cutoff are discussed. These considerations find indeed confirmation in the specific case analyzed in Section III-C. Finally, conclusions are drawn in Section V.

II. Reactive Attenuation in Lossy PPW

This section analyzes the properties of the fundamental TE-TM pair of *guided modes* supported by a *lossy* PPW. Results in this section also applies to the fundamental TE-TM pair of *leaky modes* supported by an FPC-LWA, as we will extensively demonstrate in Section III through various accurate numerical simulations.

From this standpoint, it follows that the results of this section have full generality provided that the loss tangent $\tan\delta$, here only modeling material losses, is replaced by an *equivalent* loss tangent $\tan\delta_{\rm eq}$ [15], [18], modeling radiative losses in addition to material losses. An accurate description of $\tan\delta_{\rm eq}$ for PRS-based planar waveguides is given in [18] and will be briefly commented in Section III for the reader's convenience.

In order to maintain the discussion as general as possible, the results of Section II and III are expressed in terms of a normalized frequency $\tilde{f} = f/f_0$, where f_0 corresponds to the *cutoff* frequency, i.e., the frequency for which $\beta = \alpha$.

This Section is organized in three subsections. Subsections II-A and II-B introduce the lossy PPW model and a figure of merit for the determination of reactive attenuation in lossy PPWs, whereas in Subsection II-C, significant analytical results are derived.

A. Lossy PPW model

The wavenumber dispersion of the TE-TM degenerate fundamental pair of guided modes supported by a lossy PPW has the following well-known expression [19]:

$$k_z/k_0 = \hat{k}_z = \hat{\beta} - j\hat{\alpha} = \sqrt{\varepsilon_r'}\sqrt{1 - j\tan\delta - \frac{\lambda^2}{4h^2\varepsilon_{\rm r}'}}, \quad (1)$$

where λ is the vacuum wavelength, $\varepsilon_{\rm r} = \varepsilon_{\rm r}'(1 - j\tan\delta)$ is the complex-valued dielectric permittivity of the material filling the PPW (a nonmagnetic material is assumed for simplicity), and h is the plate distance. We further assume that the plate distance is set to $h = h_{\rm ppw} = \lambda_0/2\sqrt{\varepsilon_{\rm r}'}$ to have the cutoff condition (i.e., $\beta = \alpha$), occurring exactly at the cutoff frequency $f_0 = c/\lambda_0$ (c being the speed of light in vacuum, and $\lambda_0 = \lambda|_{f=f_0}$). With this assumption, Eq. (1) reads:

$$\hat{k}_z = \sqrt{\varepsilon_r'}\sqrt{1 - j\tan\delta - \tilde{f}^{-2}}, \quad (2)$$

Dispersion curves, i.e., $\hat{\beta}$ and $\hat{\alpha}$ vs. $\tilde{f}$ for $10^{-4} \leq \tan\delta \leq 10^{-1}$ are reported in Fig. 2(a) (dispersion curves shade from dark blue to light blue as $\tan\delta$ ranges from 10^{-4} to 10^{-1}). The effect of the loss tangent is to raise the value of $\hat{\alpha}$ (or equivalently $\hat{\beta}$) at the cutoff frequency.

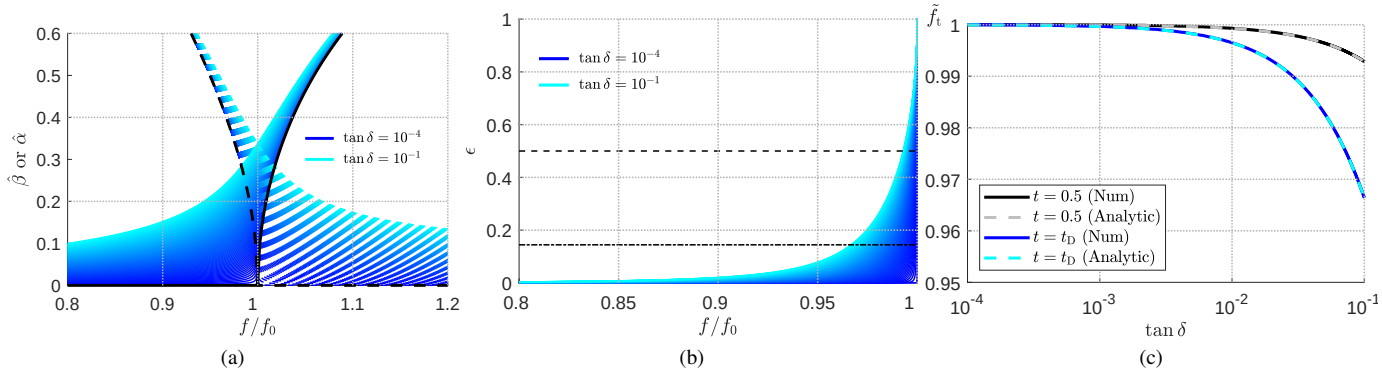

Fig. 2. Results for lossy PPWs. (a) Dispersion curves $\hat{\beta}$ (solid lines) and $\hat{\alpha}$ (dashed lines) vs. $\tilde{f} = f/f_0$ for $10^{-4} \leq \tan\delta_{\rm eq} \leq 10^{-1}$ (color shade from dark blue to light blue as $\tan\delta$ increases). (b) The figure of merit ϵ (eq. (3)) vs. $\tilde{f}$. A dashed and a dashed-dotted line mark the conditions $\epsilon = 0.5$ and $\epsilon = r_{\rm D} \simeq 0.1444$. (c) The frequencies $\tilde{f}_t|_{t=1/2}$ and $\tilde{f}_{\rm D}$ vs. $\tan\delta$ calculated through (7) (dashed cyan curve) and (9) (dashed grey curve), and their numerical evaluations (in solid black and blue curves, respectively).

B. Figure of Merit for Lossy PPWs

We recall that modal attenuation in PPWs can occur in two independent ways: one is always present and is due to the reactive attenuation experienced by modes below the cutoff frequency, and the other one is due to the presence of losses, if any. Therefore, in a *lossless* PPW, we only have reactive attenuation that is completely determined by the imaginary part of the modal wavenumber.

On the other hand, in order to determine the contribution of the reactive attenuation in a *lossy* PPW, it is useful to consider the wavenumber dispersion of a *lossless* PPW, obtained from (2) for $\tan\delta = 0$ and reported in black solid and dashed lines in Fig. 2(a). As discussed above, in the lossless case, for $\tilde{f} < 1$, the propagation wavenumber is purely imaginary $\hat{k}_{z,\rm ppw} = -j\hat{\alpha}_{\rm ppw}$ and thus accounts only for reactive attenuation, as opposed to the lossy case where $\hat{k}_z$ is generally complex and $\hat{\alpha}$ accounts for all kinds of losses.

At this point, it is convenient to define the following figure of merit

$$\epsilon = \frac{\hat{\alpha} - \hat{\alpha}_{\rm ppw}}{\hat{\alpha}}, \tag{3}$$

which quantitatively *isolate* the portion of attenuation that is not due to reactive phenomena. By definition $0 \leq \epsilon \leq 1$: for $\epsilon \to 0$, reactive attenuation dominate over other losses, and vice versa for $\epsilon \to 1$. In general, ϵ measures the portion of the attenuation constant that is not contributing to reactive attenuation. In Fig. 2(b) ϵ vs. $\tilde{f}$ is reported for the same cases analyzed in Fig. 2(a). As expected, ϵ abruptly decreases as $\tilde{f} < 1$, and the rate of decrease depends on $\tan\delta$: the lower is the $\tan\delta$ the steeper is the transition.

We note here that ϵ is intimately related to the figure of merit defined in [9, eq. (9)]; the connection between them will be evident in the next subsection.

C. Analytical Results

The simple form of (2) allows for deriving certain interesting results with a fully analytical approach. In particular, it is convenient to define

$$\hat{\alpha}_{\rm ppw} := -{\rm Im}\{\hat{k}_z\}|_{\tan\delta=0} = \sqrt{\varepsilon_r'}\sqrt{\tilde{f}^{-2} - 1}, \tag{4a}$$

$$\hat{\alpha}_{\rm c0} := -{\rm Im}\{\hat{k}_z\}|_{\tilde{f}=1} = \sqrt{\varepsilon_{\rm r}' \tan\delta/2}, \tag{4b}$$

so as to recast (2) in the following compact form

$$\hat{\alpha} = \hat{\alpha}_{\rm ppw}\sqrt{\frac{1 + \sqrt{1 + 4(\hat{\alpha}_{\rm c0}/\hat{\alpha}_{\rm ppw})^4}}{2}}, \tag{5}$$

where the frequency-dependent character of $\hat{\alpha}$ is now implicit in the definition of $\hat{\alpha}_{\rm ppw}$.

It is worth to mention here that eq. (7) in [9] is but the first-order McLaurin approximation of (5) with respect to $(\hat{\alpha}_{\rm c0}/\hat{\alpha}_{\rm ppw})^2$. (Note that the definitions of $\hat{\alpha}_{\rm ppw}$ and $\hat{\alpha}_{\rm c0}$ in (4a)–(4b) correspond to $\sqrt{|Er|}$ and $\sqrt{Ei/2}$, with $E = Er - jEi = \hat{k}_z^2$ in [9].) We should also stress that in the present work we are particularly interested in the role of reactive attenuation close to the cutoff condition where $\hat{\alpha}_{\rm ppw} \simeq \hat{\alpha}_{\rm c0}$ and thus the formulas in [9] would lead to inaccurate results (although the approximation error goes as $\mathcal{O}(\hat{\alpha}_{\rm c0}^4/\hat{\alpha}_{\rm ppw}^4)$, and thus rapidly decays far from the cutoff f_0).

Using (5) in (3) we get an analytical expression for ϵ as a function of $\tilde{f}$. Such an expression allows for easily calculating the normalized frequency $\tilde{f}_{\rm t}$ for which $\epsilon|_{\tilde{f}=\tilde{f}_{\rm t}} = t$, being t a fixed threshold. After algebraic manipulations, an analytical expression for $\tilde{f}_{\rm t}$ as a function of t is found

$$\tilde{f}_{\rm t} = \sqrt{\frac{1}{1 + \tan\delta/(2T)}}, \quad T = \frac{1}{(1-t)^2}\sqrt{t(2-t)}. \tag{6}$$

If one is interested to find the normalized frequency for which the reactive attenuation is 50% of the total attenuation (see the intersections between the colored curves and the black dashed line in Fig. 2(b)), one has to set $t = 1/2$, for which $T = 2\sqrt{3}$ and thus (6) reduces to

$$\tilde{f}_{\rm t}|_{t=1/2} = \sqrt{\frac{1}{1 + \tan\delta/(4\sqrt{3})}}. \tag{7}$$

This expression is reported in Fig. 2(c) where the analytical results (solid lines) are compared with numerical results (dashed

lines) obtained from a numerical search of the intersection points in Fig. 2(b).

Equation (5) and (6) can also be profitably used to determine the normalized frequency at which an FPC-LWA is supposed to have maximum directivity at broadside $D_{0,\max}$ [15]. (We recall here that the connection between lossy PPWs and FPC-LWAs will be clear in Section III, as mentioned in the premise to this Section II). As shown in [15], $D_{0,\max}$ occurs at a normalized frequency $\tilde{f}_{\rm D}$ for which $\hat{\beta}/\hat{\alpha} = r_{\rm D}$ with $r_{\rm D} = (\sqrt{3}-1)/\sqrt{2} \simeq 0.5176$. Taking the real part of $\hat{k}_z^2$, and exploiting the definition of $\hat{\alpha}_{\rm c0}$ (cf. (4b)), we obtain from (2) the hyperbolic relation $\hat{\beta}\hat{\alpha} = \hat{\alpha}_{\rm c0}^2$ [15] which yields

$$\hat{\alpha}|_{\tilde{f}=\tilde{f}_{\rm D}} = \hat{\alpha}_{\rm c0}/\sqrt{r_{\rm D}} \simeq 1.3899\hat{\alpha}_{\rm c0}. \tag{8}$$

This last relation (8) can be used in (5) to find $\tilde{f}_{\rm D}$. A few algebra yields:

$$\tilde{f}_{\rm D} = \frac{1}{\sqrt{1+\tan\delta/\sqrt{2}}}. \tag{9}$$

Interestingly, comparison between (6) and (9) suggests that a threshold value $t = t_{\rm D}$ exists for which $\tilde{f}_{\rm t} = \tilde{f}_{\rm D}$. Indeed, equating the two expressions, the following equation is found:

$$t_{\rm D}^4 - 4t_{\rm D}^3 + 8t_{\rm D}^2 - 8t_{\rm D} + 1 = 0, \tag{10}$$

whose only real root is $t_{\rm D} \simeq 0.1444$. Therefore, the condition for achieving maximum directivity at broadside in an FPC-LWA always occurs at a frequency point for which $\epsilon \simeq 0.1444$ (see dashed-dotted black line in Fig. 2(b)). It is worth noting that this result holds for any choice of $\tan\delta$ and $\varepsilon_{\rm r}'$, in the limit that the lossy PPW approximation holds. For the sake of completeness, analytical results for $\tilde{f}_{\rm t}$ (solid lines) are compared with numerical results (dashed lines) in Fig. 2(c). (Note that analytical results refer to the direct implementation of (7) and (9), whereas numerical results refer to the numerical search of the corresponding frequencies from results of Fig. 2(a) and (b).)

We emphasize that in the cases analyzed here (and also in practical cases) $\tan\delta \ll 1$, thus (6), (7), and (9) are well approximated by their first-order McLaurin expansions:

$$\tilde{f}_{\rm t} = 1 - \frac{\tan\delta}{4T}, \quad \tilde{f}_{\rm t}|_{t=1/2} = 1 - \frac{\tan\delta}{8\sqrt{3}}, \quad \tilde{f}_{\rm D} = 1 - \frac{\tan\delta}{2\sqrt{2}}. \tag{11}$$

The simple form of (11) highlights that $\tilde{f}_{\rm D}$ and in general $\tilde{f}_{\rm t}$ are close to the cutoff: and the lower the losses, the closer to the cutoff they are.

The analytical results of this subsection are open to different interpretations. From the definition of ϵ, it does not seem convenient to operate at $\tilde{f}_{\rm D}$, because in that region reactive attenuation may prevail on other losses mechanisms. On the other hand, a low value of ϵ is not strictly connected to the structure performance. Therefore, it is worth to further investigate what should be the minimum threshold t for ϵ. In this regard, the results of Section IV will show that $\tilde{f}_{\rm D}$ (thus $t = t_{\rm D} \simeq 0.1444$) sets a lower-bound to the normalized frequency for which a good matching can theoretically be achieved.

III. Reactive Attenuation in PRS-based Planar Waveguides

This Section specializes the general results of the previous Section II to the relevant case of PRS-based planar waveguides. Three subsections are considered: the connection between FPC-LWAs and lossy PPWs is highlighted in Subsection III-A, whereas the numerical validation of the analytical results of the previous sections is reported in Subsection III-B for several cases of PRS-based FPC-LWAs, and in Subsection III-C for the relevant case of GPWs.

A. Connection to Lossy PPWs

We refer here to a class of PRS-based planar waveguides used as basic constituents of FPC-LWAs. As shown in Fig. 1, a scalar shunt admittance $Y_{\rm s}$ is used to fully characterize the electromagnetic behavior of a PRS placed on top of the cavity. It should be stressed that, in spite of its simplicity, this approach has been proven to be rather accurate for the modeling of various kinds of PRSs in the homogenized regime [20]–[22], and even for $\lambda_0/4$ superstrate dielectric layer or distributed Bragg reflectors [18], [23].

The application of the transverse resonance technique [19], [24] to the transverse equivalent network depicted in Fig. 1(b) yields the following dispersion equations for TE and TM polarizations, respectively:

$$\hat{k}_{x0} + \bar{Y}_{\rm s} - j\hat{k}_{x\varepsilon}\cot(k_0 h\hat{k}_{x\varepsilon}) = 0, \tag{12a}$$

$$\hat{k}_{x0}^{-1} + \bar{Y}_{\rm s} - j\varepsilon_{\rm r}\hat{k}_{x\varepsilon}^{-1}\cot(k_0 h\hat{k}_{x\varepsilon}) = 0, \tag{12b}$$

where $\hat{k}_{x0} = \sqrt{1-\hat{k}_z^2}$ and $\hat{k}_{x\varepsilon} = \sqrt{\varepsilon_{\rm r}-\hat{k}_z^2}$ are the normalized vertical wavenumbers in free-space and in the dielectric, respectively, and $\bar{Y}_{\rm s} = Y_{\rm s}\eta_0 = \bar{G}_{\rm s} + j\bar{B}_{\rm s}$ is the (generally complex) admittance normalized to the free-space impedance $\eta_0 \simeq 377\,\Omega$. The fundamental TE and TM leaky mode pair is found searching for the complex improper (i.e., $\mathrm{Im}\{k_{x0}\} > 0$) roots of (12a) and (12b). Although the dispersion curves of the TE and TM leaky modes are generally different (as a consequence of the different expression of their respective dispersion equations), they can accurately be represented by the wavenumber dispersion in (1) provided that the PRS is sufficiently reflective (i.e., $\bar{B}_{\rm s} \gg 1$ and $\bar{G}_{\rm s} \ll \bar{B}_{\rm s}$). It is manifest that, in the limit of $|Y_{\rm s}| \to \infty$, both (12a) and (12b) recover (2), for $h = h_{\rm ppw}$. Conversely, for finite values of $\bar{Y}_{\rm s}$, the cutoff of the TE-TM leaky mode pair is frequency-shifted in amounts that mainly depend on $|\bar{B}_{\rm s}|$ [22]. However, the cavity thickness h can be adjusted to an *equivalent* cavity height $h_{\rm eq}$ to have the TE-TM cutoffs at f_0. This can easily be obtained from either (12a) or (12b) in the limit $\hat{k}_z \to 0$ (and in turn $\hat{k}_{x0} \to 1$, $\hat{k}_{x\varepsilon} \to \sqrt{\varepsilon_{\rm r}}$) and yields:

$$h_{\rm eq} = h_{\rm ppw}\left\{1 \pm \mathrm{Re}\left[\frac{1}{\pi}\mathrm{arccot}\left(\frac{|\bar{B}_{\rm s}| \mp j(\bar{G}_{\rm s}+1)}{\sqrt{\varepsilon_{\rm r}}}\right)\right]\right\}, \tag{13}$$

where the choice of the $\pm$ and $\mp$ signs depend on the sign of $\bar{B}_{\rm s}$ (the upper/lower choice for positive/negative $\bar{B}_{\rm s}$). At this point, in order to have a complete analogy with the guided modes of a lossy PPW, we only need to model the losses (of either radiative or ohmic nature) introduced by the PRS

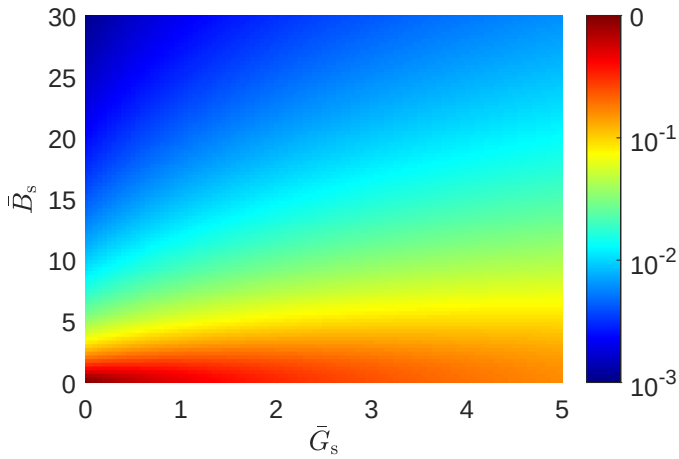

Fig. 3. Equivalent loss tangent (in logarithmic scale) as a function of $\bar{G}_\mathrm{s}$ and $\bar{B}_\mathrm{s}$, assuming $\varepsilon_\mathrm{r} = 2.3$. A nonzero dielectric loss tangent would shift the color scale.

through the definition of an *equivalent* loss tangent $\tan\delta_\mathrm{eq}$. An accurate model for $\tan\delta_\mathrm{eq}$ has been proposed in [18] and is reported here for the reader's convenience:

$$\tan\delta_\mathrm{eq} = \tan\delta + \frac{2\sqrt{\varepsilon'_\mathrm{r}}}{\pi(1+\bar{B}_\mathrm{s}^2)}\left[1 + \frac{\bar{G}_\mathrm{s}(\bar{B}_\mathrm{s}^2 - 1 - \bar{G}_\mathrm{s})}{\bar{B}_\mathrm{s}^2 + (1+\bar{G}_\mathrm{s})^2}\right] \quad (14)$$

Typical values of $\tan\delta_\mathrm{eq}$ for various choices of $\bar{G}_\mathrm{s}$ and $\bar{B}_\mathrm{s}$ are reported in Fig. 3 as a contour plot, assuming $\varepsilon'_\mathrm{r} = 2.3$ and $\tan\delta = 0$ without loss of generality (different values of ε'_r and $\tan\delta$ would simply change the dynamic range of the colormap [18]).

With these equations at hand, one can conclude that the TE-TM leaky modes of a PRS-based FPC-LWA of thickness h_eq given by (13) can accurately be characterized by the wavenumber dispersion in (2), provided that the materials constituting the structure (i.e., the complex-valued quantities ε_r and $\bar{Y}_\mathrm{s}$) are modeled through the equivalent loss tangent in (14). The accuracy of the model will be validated in the next Subsection.

B. Numerical Validation

The dispersion curves for the fundamental TE-TM leaky mode pair of an FPC-LWA with cavity height h_eq given by (13) have been obtained in Fig. 4(a) and (e) by numerically solving for the complex improper roots of (12a)–(12b) (the Padé algorithm is employed for the numerical results [25]) assuming a lossless case (see Fig. 4(a)), i.e., with $\varepsilon_\mathrm{r} = 2.3$ and $\bar{Y}_\mathrm{s} = -j\bar{B}_\mathrm{s}$ and a lossy case (see Fig. 4(e)), i.e., with $\varepsilon_\mathrm{r} = 2.3(1 - j0.01)$ and $\bar{Y}_\mathrm{s} = 5 - j\bar{B}_\mathrm{s}$ for $5 \le \bar{B}_\mathrm{s} \le 30$. This range of variation is consistent with the typical impedance values shown by conventional homogenized PRS constituted by either cermet-like (e.g., patches) or fishnet-like (e.g., strip gratings) topologies (see, e.g., [20], [22]).

The color of the TE (TM) dispersion curves shade from blue (red) to cyan (yellow) as $\bar{B}_\mathrm{s}$ ranges from 30 (high reflectivity) to 5 (low reflectivity). As expected, the TE and TM dispersion curves are always almost overlapped (the bluish curves are barely distinguishable from the reddish ones) except for very low values of $\bar{B}_\mathrm{s}$ for which the lossy PPW is no longer expected to provide for an accurate approximation because of the poor reflectivity of the PRS. For $\bar{B}_\mathrm{s} = \bar{G}_\mathrm{s} = 5$, corresponding to the brightest cyan and yellow curves in Fig. 4(e), we are indeed far from the hypotheses $\bar{B}_\mathrm{s} \gg 1$ and $\bar{G}_\mathrm{s} < \bar{B}_\mathrm{s}$.

TABLE I
VALUES OF $\tan\delta_\mathrm{eq}$ FOR CASES DISCUSSED IN SUBSECTION III-B.

Case	$\tan\delta_\mathrm{eq}$
$\bar{Y}_\mathrm{s} = -j30$, $\varepsilon_\mathrm{r} = 2.3$	0.001072
$\bar{Y}_\mathrm{s} = -j5$, $\varepsilon_\mathrm{r} = 2.3$	0.037134
$\bar{Y}_\mathrm{s} = 5 - j30$, $\varepsilon_\mathrm{r} = 2.3(1 - j0.01)$	0.016188
$\bar{Y}_\mathrm{s} = 5 - j5$, $\varepsilon_\mathrm{r} = 2.3(1 - j0.01)$	0.104965

Nevertheless, the analytical wavenumber dispersion provided in (2) (upon replacing $\tan\delta$ with $\tan\delta_\mathrm{eq}$ given in (14)) furnishes a very good approximation of the numerical TE and TM dispersion curves over the whole considered range, as can be intuitively inferred by comparing Fig. 4(a) and (e) with Fig. 2 with the aid of Table I. (We preferred not to overlap the analytical results in Fig. 4 for the sake of clarity; such a comparison will be provided in the next subsection III-C.) It is also worth noting that the cutoff condition occurs exactly at f_0 for 'large' $\bar{B}_\mathrm{s}$ and in its close proximity for 'small' $\bar{B}_\mathrm{s}$, thus validating (13).

We are now interested in addressing the consistency of (9), i.e, the analytical formula for the frequency $\tilde{f}_\mathrm{D}$ at which the broadside directivity D_0 is maximized, for the same cases presented in Fig. 4(b) and (f). To this aim, we first evaluated D_0 vs. $\tilde{f}$, in the range $0.9 \le \tilde{f} < 1$, i.e., below cutoff, (see Fig. 4(b) and (f)) calculating D_0 as [26]:

$$D_0 = \pi^2 / \left(\Delta\theta^\mathrm{E}\Delta\theta^\mathrm{H}\right), \quad (15)$$

where $\Delta\theta^\mathrm{E}(\Delta\theta^\mathrm{H})$ is the half-power beamwidth on the principal E-(H-) plane, whose general expression for $\hat{\beta} < \hat{\alpha}$ is [15], [17]:

$$\Delta\theta = 2\arcsin\sqrt{\hat{\beta}^2 - \hat{\alpha}^2 + \sqrt{2(\hat{\beta}^4 + \hat{\alpha}^4)}}, \quad (16)$$

using the value of α in the TE (TM) case for $\Delta\theta^\mathrm{E}(\Delta\theta^\mathrm{H})$.

In Fig. 4(b) and (f) D_0 is numerically evaluated from (15) and (16) using the values of β and provided in Fig. 4(a) and (e) for the TE and the TM case (in Fig. 4(b) and (f) the color of the curves shade from black to green as $\bar{B}_\mathrm{s}$ ranges from 30 to 5). The maximum directivity condition $D_{0,\max}$ is then numerically evaluated (see the colored circles) and compared with the analytical results given by (15) and (16) using the values of β and α given by (2). The excellent agreement between analytical and numerical results further confirms the accuracy of the proposed lossy PPW model.

The frequency $\tilde{f}_\mathrm{D}$ vs. $\bar{B}_\mathrm{s}$ is then retrieved from the numerical evaluation of $D_{0,\max}$ and is reported in Fig. 4(c) and (g) (see dashed green curve) where it is compared with (9) (see solid black curve). For the sake of completeness, we reported the curves that would have been obtained considering the *theoretical* $D_{0,\max}$ condition, i.e., the frequency at which

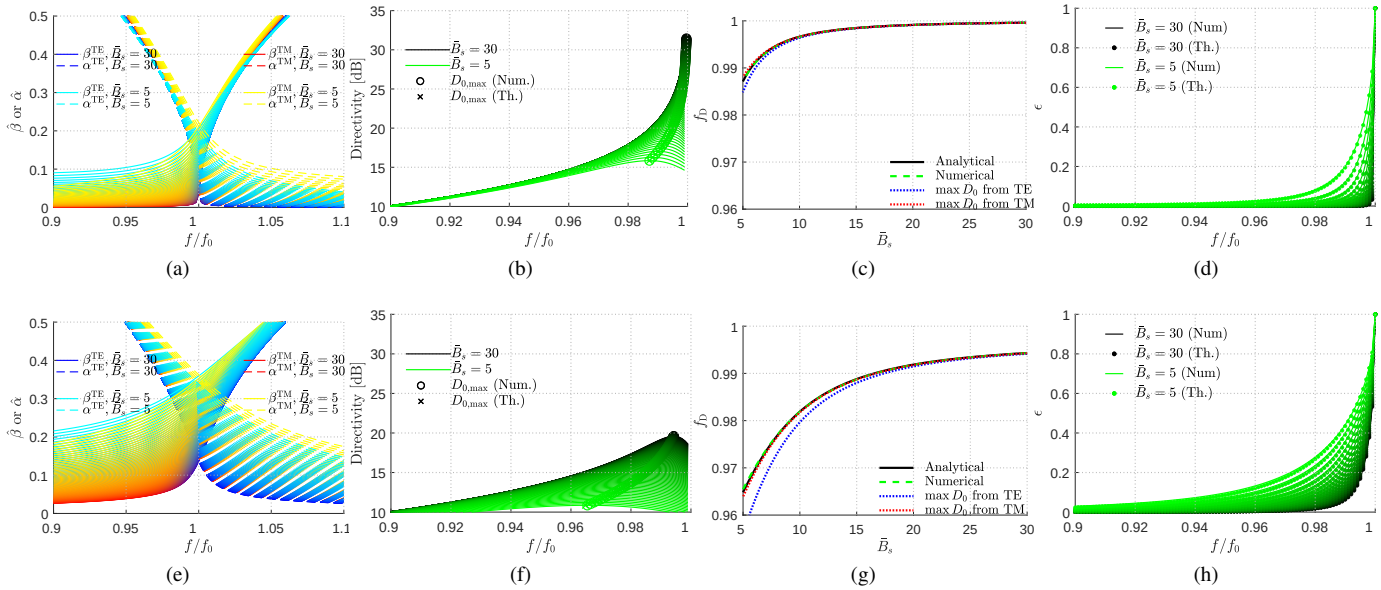

Fig. 4. Results for PRS-based FPC-LWAs with $\varepsilon_r' = 2.3$ and $5 \leq \bar{B}_s \leq 30$, for (a)–(d) a *lossless* case (viz., $\tan\delta = 0$, $\bar{G}_s = 0$), and (e)–(h) a *lossy* case (viz., $\tan\delta = 0.01$, $\bar{G}_s = 5$). In (a) and (e) the TE and TM dispersion curves $\hat{\beta}$ (solid lines) and $\hat{\alpha}$ (dashed lines) vs. $\tilde{f}$ for $5 \leq \bar{B}_s \leq 30$ (color shade from dark blue (red) to light blue (yellow) as $\bar{B}_s$ decreases in the TE (TM) case). In (b) and (f) the directivity vs. $\tilde{f}$ is numerically evaluated (solid curves) through (15) and (16) for $5 \leq \bar{B}_s \leq 30$ (the color shades from green to black as $\bar{B}_s$ increases). The maximum directivity condition is evaluated either numerically (colored circles) or analytically (colored crosses) according to the procedure described in the text. In (c) and (g) $\tilde{f}_D$ vs. $\bar{B}_s$ is numerically evaluated (green dashed curve) and compared with the analytical result of (9) (black solid curve). Results obtained from the numerical search of the maximum directivity condition (i.e., $\hat{\beta}/\hat{\alpha} = r_D$) from the TE and TM dispersion curves are also reported as dotted blue and red curves, respectively. In (d) and (h) ϵ vs. $\tilde{f}$ is calculated either numerically (solid colored lines) or analytically (colored dots) for $5 \leq \bar{B}_s \leq 30$ (the color shades from green to black as $\bar{B}_s$ increases).

$\hat{\beta}/\hat{\alpha} = r_D$ for both the TE and TM case (see dotted blue and red curves, respectively). Indeed, the *theoretical* $D_{0,\max}$ condition assumes that $\bar{B}_s \gg 1$ for which the TE-TM disequalization is negligible. However, the agreement between all curves even for small values of $\bar{B}_s$ confirm that the proposed model is remarkably accurate, even under operating conditions where it is not supposed to work well. It is also worth noting that the TM curve is almost overlapped to both the analytical and the numerical curve, whereas the TE curve is slightly different, especially for low $\bar{B}_s$. This is also in agreement with the results of Fig. 4(a) and (e) where it is seen that the TE-TM disequalization is more prominent for low $\bar{B}_s$ and $\tilde{f} < 1$. (In this range, the approximation $\hat{k}_{x0} \to 1$ used to derive (13) and (14) is more critical for TE modes where the dispersion equation has a k_{x0} term [cf. (12a)], rather than for TM modes where the dispersion equation has a $1/k_{x0}$ term [cf. (12b)].)

To complete the picture, ϵ is calculated in Fig. 4(d) and (h). Numerical results (colored solid lines) refer to the evaluation of (3) using the average between the TE and TM values of $\hat{\alpha}$ (i.e., $\hat{\alpha} := (\hat{\alpha}_{TE} + \hat{\alpha}_{TM})/2$) reported in Fig. 4(a) and (d), whereas the analytical results (colored dots) refer to the evaluation of (3) using eqs. (4a) and (4b) replacing $\tan\delta$ with $\tan\delta_{eq}$. From the comparison between either Fig. 4(c) and (d) or Fig. 4(g) and (h), it can be inferred that $\epsilon \simeq 0.1444$ for $\tilde{f}_D$, as we derived at the end of subsection II-C.

C. Application to GPWs

In the previous subsection we have numerically validated all the analytical results derived in Section II to demonstrate the consistency and accuracy of the lossy PPW model for the analysis of planar waveguides based on PRSs. The PRSs were modeled as scalar shunt complex-valued admittances with normalized susceptances and conductances ranging from 5 to 30 and from 0 to 5, respectively. We now want to use a more realistic model for the PRS in order to apply our results to cases with practical applications.

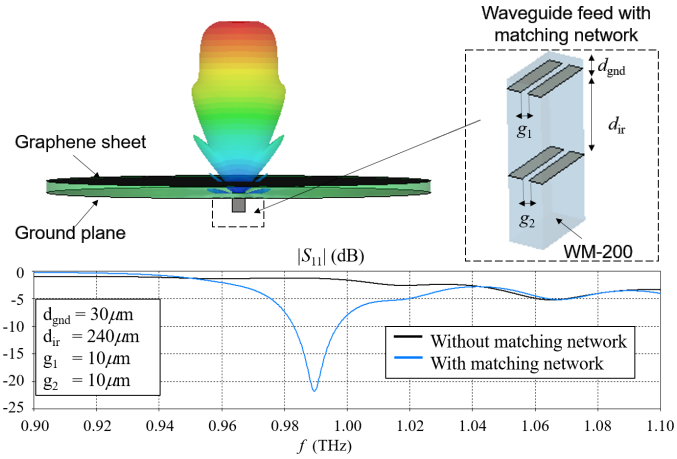

Fig. 5. (Top) A pictorial representation of a waveguide-fed GPW radiating a pencil beam at broadside and the details of the matching network (consisting of two symmetric capacitive irises) embedded in the waveguide feed to obtain impedance matching below cutoff. The waveguide feed is a standard WM-200 [27] (details in the text). (Bottom) $|S_{11}|$ vs. f of the considered structure with (light blue solid line) and without (black solid line) the matching network depicted above.

Specifically, we discuss the case of a GPW operating in the THz range similar to those analyzed in [18], [28]. The structure

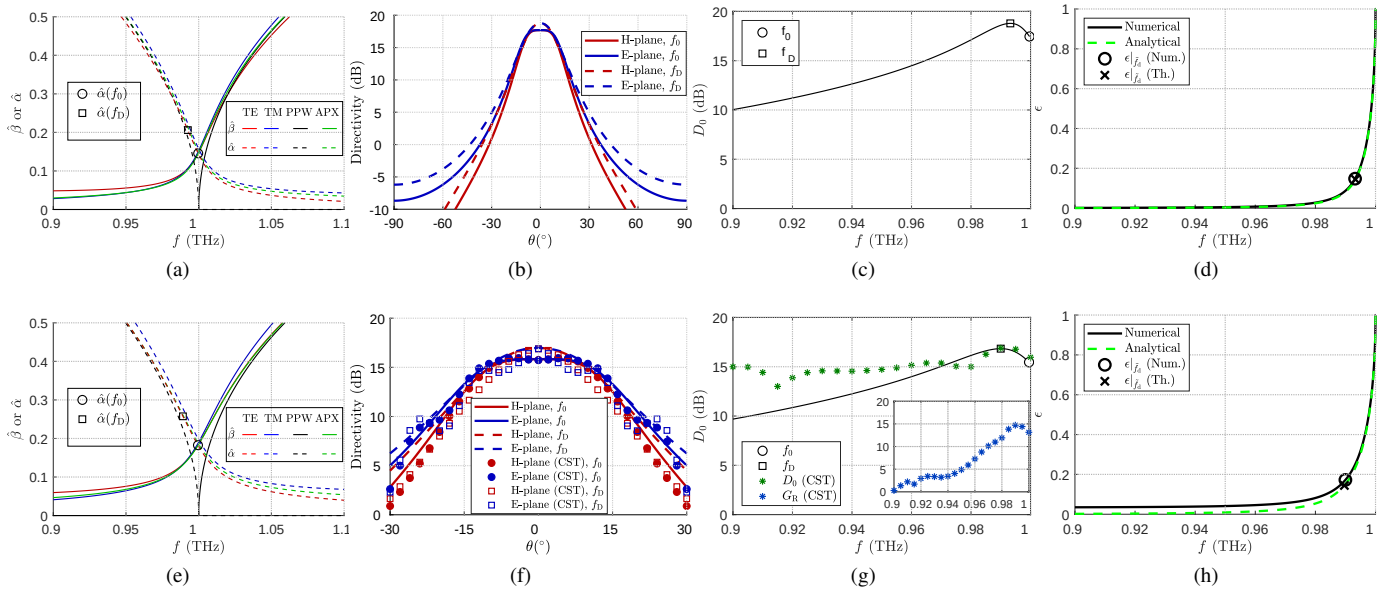

Fig. 6. Results for GPWs for (a)–(d) a *lossless*, *nondispersive* case (viz., $\bar{Y}_g = -j\bar{B}_{\rm g}|_{f=f_0}$), and (e)–(h) a *lossy*, *dispersive* case (viz., $\bar{Y}_g(f) = \bar{G}_{\rm g}(f) - j\bar{B}_{\rm g}(f)$). In (a) and (e) the TE (in red) and TM (in blue) dispersion curves $\hat{\beta}$ (solid lines) and $\hat{\alpha}$ vs. f are compared with the *lossless* PPW exact dispersion curve (in black) and the *lossy* PPW approximate dispersion curve (in green). The cutoff and $D_{0,\max}$ conditions are highlighted with a black circle and a black square, respectively. In (b) and (f) the directivity patterns vs. θ along the principal planes have been calculated at f_0 (solid red and blue curves for the H- and E-plane, respectively) and at $f_{\rm D}$ (dashed red and blue curves for the H- and E-plane, respectively). In (f) full-wave results for the structure depicted in Fig.5 are reported in small colored circles (for $f = f_0$) and squares (for $f = f_{\rm D}$). In (c) and (g) the directivity at broadside D_0 vs. f is numerically evaluated. The cutoff and $D_{0,\max}$ conditions are highlighted with a black circle and a black square, respectively. In (g) CST full-wave results for the structure depicted in Fig. 5 are reported as green asterisks. The inset shows the realized gain $G_{\rm R}$ vs. f obtained from full-wave simulations. In (d) and (h) ϵ vs. f is calculated either numerically (solid black line) or analytically (dashed green line). The $D_{0,\max}$ condition as per numerical or analytical evaluation is highlighted with a black circle or a black cross.

is designed to 'resonate' at $f_0 = 1$ THz and consists of a GDS made of TOPAS ($\varepsilon'_{\rm r} = 2.3$, $\tan\delta = 0.004$ [29]), covered with a uniform graphene sheet biased at $\mu_{\rm c} = 1$ eV. Application of (13) for the case analyzed here fixes the substrate thickness to around $92\,\mu$m (the normalized surface admittance of the graphene sheet is provided next). The structure is excited from the back by etching a quasi-resonant slot $200\mu{\rm m} \times 100\mu{\rm m}$, around $\lambda_0/3 \times 2\lambda_0/3$ at $f_0 = 1$ THz, which is equivalent to a horizontal magnetic dipole-like source that excites both the TE and TM leaky modes required to radiate a pencil beam at broadside [30]. The slot is then fed through a standard WM-200 rectangular waveguide [27], that has the same dimensions of the slot and operates in the range $0.9 - 1.4$ THz.

Due to the resonant character of the cavity, impedance matching can be difficult, especially below cutoff where the wave impedance exhibits a predominantly reactive behavior [31] (see next Section IV). As a consequence, an ad hoc impedance matching network is usually required. In this regard, we recall that networks consisting of capacitive irises have been proven to be effective for matching waveguide feeds in FPC-LWAs radiating beyond the cutoff frequency [32]–[36]. Here, we use a technique similar to that presented in [32], obtaining a good impedance matching below cutoff by optimizing the distance and the geometric features of two capacitive irises [37] (optimized design parameters are provided in Fig. 5), as shown by the CST full-wave results [38] reported in Fig. 5 for the reflection coefficient of the structure with and without the optimized matching network.

It is worth to point out that, since we were interested in analyzing the radiation performance close to the cutoff condition, we preferred to drive the full-wave optimization to achieve a lower reflection coefficient (lower than -10 dB) over a narrower fractional bandwidth (around 2%). Nevertheless, a wider impedance matching can be achieved still respecting the Bode-Fano criterion [39], [40]. Here, the choice we made also accounted for the fabrication tolerances of large-area photolithographic processes that limits the smallest detail (here dictated by the iris gap that is around $10\,\mu$m) to be not lower than $3\,\mu$m [41].

There are several reasons for the choice of a graphene sheet as a homogenized PRS that are worthy to be commented. First, graphene is a lossy PRS whose normalized surface admittance $\bar{Y}_{\rm g} = \bar{G}_{\rm g} + j\bar{B}_{\rm g}$ is known in closed-form [42]. (Specifically, we modeled graphene using Kubo formula for $\mu_{\rm c} = 1$ eV, $\tau = 3$ ps, $T = 300$ K as in [28], [43], [44]).

Even more interestingly, in the low THz regime, graphene shows the same Drude-like expression for both TE and TM polarizations, exhibits negligible TE-TM modal coupling and negligible spatial dispersion (the dependence from the propagation wavenumber) [43], [45], thus the dyadic expression that would arise from the application of the generalized sheet transition conditions [46] reduces to a single frequency-dependent *scalar* expression. Furthermore, the behavior of graphene at THz and for $\mu_c = 1$ eV (as modeled here) is more reactive than resistive (i.e., $\bar{B}_{\rm g} > \bar{G}_{\rm g}$), thus the value of $\bar{Y}_{\rm g}(f)$ at f_0 ($\bar{Y}_{\rm g0} = \bar{Y}_{\rm g}(f_0) = 0.37 - j7.04$) is fully within the range of the cases analyzed in III-B. We note that, although the model proposed in III-A does not account for the inherent

frequency-dispersive behavior of $\bar{Y}_{\rm g}(f)$, the dispersion and radiation features of the leaky modes propagating in a GPW are mainly determined by the value of $\bar{Y}_{\rm g0}$ [18].

For this purpose, we here analyze the structure described above under two circumstances. In the first case, numerical results are obtained ignoring dielectric losses (i.e., $\tan\delta = 0$) and modeling graphene as a lossless, nondispersive PRS, i.e., replacing $\bar{Y}_{\rm s}$ with $j\bar{B}_{\rm g0}$. In this situation, results are a particular case of those reported in Figs. 4(a)–(d). In the second case, numerical and CST full-wave results are obtained accounting for all kinds of losses and modeling graphene as a lossy, dispersive PRS, i.e., replacing $\bar{Y}_{\rm s}$ with $\bar{Y}_{\rm g}$. This case allows us to determine in what extent the frequency-dispersive character of a PRS affects our approximation.

Results for the first and the second case are shown in Figs. 6(a)–(d) and Figs. 6(e)–(h), respectively. In Fig. 6(a) and (e) the dispersion curves for the TE and TM modes (in red and blue, respectively) are now compared with the analytical results for an equivalent lossless PPW (in black) and a lossy PPW (in green). As is manifest, the lossy PPW model is remarkably accurate in both cases. A black circle and a black square identify the cutoff $\hat{\alpha}(f_0)$ and the maximum broadside directivity conditions $\hat{\alpha}(f_{\rm D})$, as predicted by the analytical formulas provided in Section II. The directivity patterns along the principal planes evaluated at f_0 and $f_{\rm D}$ (calculated by taking advantage of the closed-form asymptotic expressions for the leaky radiation patterns, see, e.g., [15]) are reported in Fig. 6(b) and (f), whereas the variation of the broadside directivity D_0 vs. f is reported in Fig. 6(c) and (g). These results confirm that D_0 is actually enhanced for $f = f_{\rm D}$.

For the second case only, i.e., in the lossy, frequency-dispersive case, full-wave results of the entire structure depicted in Fig. 5 are overlapped to those obtained through the asymptotic expressions in Fig. 6(f) and (g). Comparison between full-wave and asymptotic results reveals an excellent agreement for the radiation patterns, where a 1-dB directivity enhancement at $f_{\rm D}$ is manifest with respect to the directivity at f_0. A poor agreement is instead observed for frequencies far from the cutoff, but this is fully compatible with the fact that radiation at these frequencies is no longer dominated by the leaky-wave pattern [47], [48], and the directivity patterns obtained through the full-wave simulations are not accurate due to the negligible amount of radiated power. In this regard, we have also verified (see the inset of Fig. 6(g)) that far from cutoff, approximately for $f/f_0 < 0.96$, the total efficiency abruptly decreases and in turn the realized gain $G_{\rm R}$ drops to values as low as few dB, thus compromising the antenna performance in this frequency range. It is worth noting that the maximum realized gain is around 2 dB smaller than the maximum directivity, in good agreement with the total efficiency that is predicted by the formulas in [18] (based on the equivalent tangent model) which yields 64% (around 61% from full-wave simulations).

Furthermore, it is worth to comment on the effects of the lateral truncation. As a matter of fact, the condition for maximizing directivity at broadside is derived for an infinite structure [15], whereas the one simulated here has a diameter of $L = 10\lambda_0$ which leads to an aperture efficiency of around 99.99% through the formula $\eta = 1-\exp(-\alpha L)$ [3]. We noted that when we set the lateral truncation to have $\eta = 90\%$ as recommended in reference books on LWAs [49]–[51] the full-wave simulation returned a broadside directivity that is no longer maximized at $f_{\rm D}$ but at f_0. This result is related to two different aspects. On one hand, the antenna finite size has effects on the radiation pattern that may lead to results that differ from those predicted by the theory, as shown for 1-D bidirectional LWAs [16], [17]. On the other hand, the full-wave simulation does not account for the presence of an absorber at the lateral edge, and thus spurious unwanted reflections affect the radiation patterns (the interested reader can find more details about the effect of the lateral edge truncation in [52], [53]). Therefore, for the correct full-wave analysis of this class of antennas it is important to set a lateral truncation larger than that recommended in classical books [49]–[51]. For the case analyzed here we noted that $\eta > 99.99\%$ is usually sufficient to provide for accurate results.

TABLE II
VALUES OF $f_{\rm D}$ FOR THE CASES DISCUSSED IN SUBSECTION III-C.

Method	lossless, nondisp.	lossy, nondisp.	lossy, disp.
$\tilde{f}_{\rm D}$, Eq. (9)	0.99331	0.98963	0.98963
$\tilde{f}_{\rm D}$ (Num.)	0.99320	0.98946	0.98998
$\tilde{f}_{\rm D}$ (Num. TE)	0.99256	0.98830	0.98916
$\tilde{f}_{\rm D}$ (Num. TM)	0.99346	0.98980	0.99052

The figure of merit ϵ is finally shown in Fig. 6(d) and (h). As expected, the numerical (in solid black line) and analytical (in dashed green line) results are overlapped over the shown frequency range for the lossless, nondispersive case (see Fig. 6(d)) and are just barely different for $\tilde{f}$ far from cutoff, in the lossy, dispersive case (see Fig. 6(h)). In order to better understand what is the sole effect of the frequency dispersion, we have also analyzed a lossy, nondispersive case (not shown for brevity) for which we report some relevant numerical results in Table II. There, results labeled as 'Num. TE/TM', refer to the numerical evaluation of $\tilde{f}_{\rm D}$ from the TE/TM dispersion curves, searching for the frequency point for which $\hat{\beta}/\hat{\alpha} = r_{\rm D}$. The slight difference between the two values are due to the TE-TM disequalization. Remarkably, from Table II we note that the analytical formula for the prediction of $\tilde{f}_{\rm D}$ is accurate up to the third decimal place in all cases, thus the frequency-dispersive character of the PRS is negligible.

IV. IMPEDANCE MATCHING CONSIDERATIONS

The theoretical results analytically derived in Section II and numerically validated in Section III revealed that the condition for achieving maximum broadside directivity occurs in a region where the reactive effects are supposed to prevail on radiative effects. On one hand, a low value of ϵ corresponds to a wave impedance $Z_{\rm w}$ with a rather reactive behavior which may hinder the impedance matching of a structure. On the other hand, although requiring ad hoc impedance matching networks, a structure operating in a regime exhibiting a low

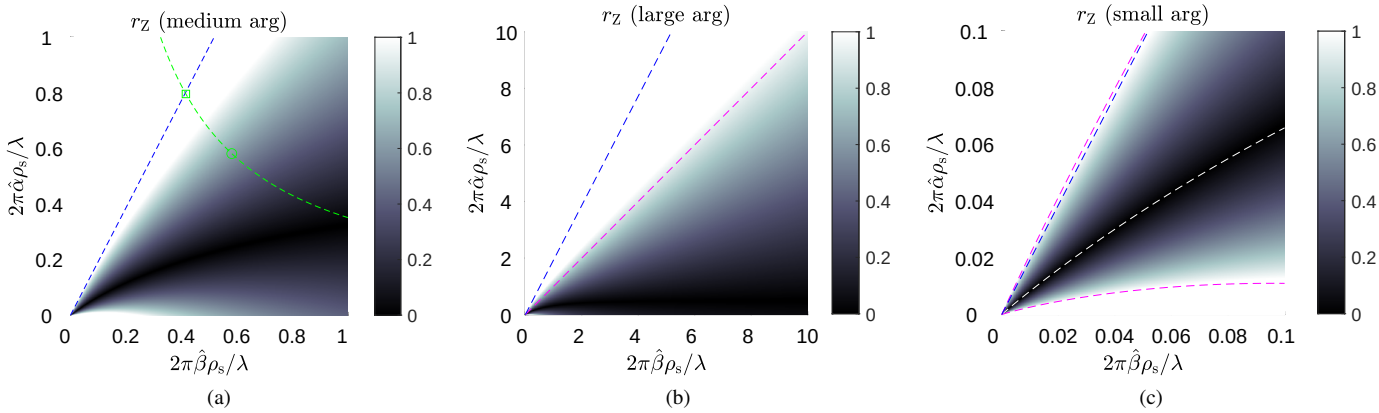

Fig. 7. Grayscale maps displaying r_Z over the complex z^*-plane for (a) $|z^*| \leq 1$, (b) $|z^*| \leq 10$ (large arguments), and (c) $|z^*| \leq 0.1$ (small arguments), assuming $\rho_s = \lambda_0/2$ at $f_0 = 1$THz. The dashed blue lines highlight the $\hat{\beta}/\hat{\alpha} = r_D$ trajectory, whereas the dashed magenta and white lines highlight the $r_Z = 1$ and $r_Z = 0$ trajectories, respectively. In (a) the dashed green hyperbola represents the approximate dispersion curve of the GPW (i.e., the green curve in Fig. 6(e)); a green circle and a green square highlight the cutoff and $D_{0,\max}$ conditions on the curve.

ϵ can still work properly as demonstrated in subsection III-C. However, the results obtained in subsection III-C are a particular case, whereas it would be interesting to derive more general results that do not depend on the type of the feed, neither on the PRS.

For this purpose, we are interested here to determine a practical lower bound to ϵ on the basis of a rigorous evaluation of the wave impedance ratio $r_Z = |\mathrm{Im}[Z_w]|/|\mathrm{Re}[Z_w]|$, a figure of merit that has been introduced in [31, Sec. 5.3, p. 211] to define the *gradual cutoff* of higher-order guided modes (thus characterized by *real* wavenumbers) in radial waveguides, and that has been recently extended to leaky modes (thus characterized by *complex* wavenumbers) in PRS-based planar waveguides [54]. However, [54] only discusses higher-order cylindrical leaky modes, i.e., leaky modes showing an azimuthal phase variation of the kind $\exp(-j\ell\phi)$, ℓ being the nonzero azimuthal integer order. Conversely, we are here interested in zeroth-order cylindrical leaky modes. Specifically, we want to find conditions for which $r_Z = 0$ (resistive impedance) and $r_Z = 1$ (reactive impedance), when the zeroth-order leaky modes supported by a PRS-based planar waveguides are excited by an elementary source feed of radius ρ_s.

To this aim and without loss of generality, we consider the expression of the TM wave impedance of a zeroth-order leaky mode (r_Z is equal for the TE and TM case [31], [54]), which is proportional to the ratio between $a = -jzH_0^2(z)$ and $b = H_0^{(2)'}(z)$, where $H_0^{(2)}$ ($H_0^{(2)\prime}$) are the (derivative of the) zeroth-order Hankel function of the second kind and $z = 2\pi\hat{k}_z\rho_s/\lambda$. With this expression at hand, it can be shown [54] that the $r_Z = 0$ and $r_Z = 1$ conditions yield,

$$r_Z = 0 \quad \text{for} \quad \angle a - \angle b = \pm m\pi, \tag{17a}$$

$$r_Z = 1 \quad \text{for} \quad \angle a - \angle b = \pm\pi/4 \pm m\pi/2, \quad m \in \mathbf{Z}. \tag{17b}$$

While (17a) and (17b) generally require a numerical evaluation that is reported in Fig. 7(a) as a contour plot over the complex z^*-plane (the conjugate is taken to be consistent with the definition of $\hat{\alpha} = \mathrm{Im}[z]$) for $|z| \leq 1$, approximate analytical results can be found in the asymptotic limit of $z \to 0$ (electrically small feed) and $z \to \infty$ (electrically large feed), taking advantage of the asymptotic expansions of small and large arguments for Hankel functions.

For large arguments, the asymptotics of $H_\ell^{(2)}(z)$ is the same for any ℓ (except for an irrelevant phase term), thus the results obtained for $\ell > 0$ in [54] also hold for this case. The evaluation of r_Z for $|z| \leq 10$ is reported in Fig. 7(b) and reveals that the condition for achieving maximum D_0 $\hat{\alpha}/\hat{\beta} = 1/r_D$ (marked as a dashed blue line) lies well beyond the $r_Z = 1$ condition (marked as a dashed magenta line). Indeed, for large arguments it has been found [54] that the $r_Z = 1$ loci lies on the trajectory $\angle z^* = \pi/4$, whereas the trajectory of maximum D_0 corresponds to $\angle z^* = \pi/2 - \arctan(r_D) \simeq 62.6°$.

Conversely, for small arguments, results of [54] cannot be extended to $\ell = 0$ due to the different asymptotic behavior of the Hankel functions [55]. After few steps and using that $H_0^{(2)}(z) \sim 1 - 2j\ln z/\pi$ (note the presence of the constant term as opposed to the conventional small argument approximation that only retains the leading term [56, eq. (9.1.8)]) we get that the loci of $r_Z = 0$ and $r_Z = 1$ are implicitly defined by the following equations:

$$r_Z = 0 \quad \text{for} \quad \frac{\cot(2\angle z)}{\pi/2 + \angle z} = \frac{1}{\ln|z|}, \tag{18a}$$

$$r_Z = 1 \quad \text{for} \quad \frac{\cot(2\angle z \pm (2m+1)\pi/4)}{\pi/2 + \angle z} = \frac{1}{\ln|z|}. \tag{18b}$$

The trajectories given by these two equations (marked as dashed magenta and white lines, respectively) are reported in Fig. 7(c) where r_Z is evaluated for $|z| < 0.1$. From both (18a) and (18b) and Fig. 7(c), it can be inferred that for very small $|z|$, the trajectories of $r_Z = 0$ and $r_Z = 1$ converge to $\angle z^* = \pi/4$ and $\angle z^* = \pi/8, 3\pi/8$, respectively, thus recovering the results obtained for $\ell \neq 0$ (and that would be obtained here by neglecting the constant term in the small argument asymptotic expansion of $H_0^{(2)}(z)$).

Interestingly, the trajectory of maximum D_0, viz., $\angle z^* \simeq 62.6°$ now lies slightly below the $r_Z = 1$ condition, viz., $\angle z^* \simeq 67.5°$, thus revealing that in this region reactive

effects are slightly lower than resistive effects, and thus impedance matching, although difficult, is not impractical.

Just to give an example, we reported in Fig. 7(a) the dispersion curve (in green dashed line) of the GPW studied in III-C over the z^*-plane assuming $\rho_\mathrm{s} = \lambda_0/2 = 150\ \mu\mathrm{m}$ (at $f_0 = 1$ THz) which is the average of the waveguide feed dimensions. The maximum D_0 and cutoff conditions have been highlighted with a green square and a green circle. As expected, the wavenumber dispersion defines a hyperbolic curve over the z^*-plane [15], and $\tilde{f}_\mathrm{D}$ and $\tilde{f}_0$ lie along the $\angle z^* \simeq 62.6^\circ$ and $\angle z^* \simeq 45^\circ$ trajectories, respectively. As can be seen, for this choice of ρ_s, Fig. 7(a) predicts a poor impedance matching in spite of the satisfactory results obtained in subsection III-C (see Fig. 5).

Nonetheless, we should admit that while we have been able to easily match the antenna *beyond* the cutoff frequency (results are not shown for the sake of conciseness), the configuration provided in subsection III-C and capable of providing matching *below* the cutoff frequency, resulted from an extensive optimization of the design parameters. In particular, we noted that matching below cutoff required highly capacitive irises (thus very small iris gaps) in order to compensate for the predominantly reactive character of the wave impedance.

However, while a general criterion cannot be formulated from the analysis of r_Z solely, it can still be concluded that any operating frequency f_op in the range $f_\mathrm{D} < f_\mathrm{op} < f_0$ offers a good compromise between the radiating performance (optimized for f_op closer to f_D) and the impedance matching (easier for f_op closer to f_0).

V. Conclusion

In this work, we have carefully analyzed the role of reactive attenuation close to the cutoff condition for leaky modes propagating in planar open waveguides based on partially reflecting surfaces, which are also the basic constituents of Fabry–Perot cavity leaky-wave antennas. In particular, we have exploited the analogy between the leaky modes supported by such structures and the guided modes propagating in lossy parallel-plate waveguides and to derive useful approximate analytical formulas.

Specific emphasis has been given to the region below the cutoff condition where a significant figure of merit has been introduced to quantitatively assess the contribution of reactive attenuation and that of attenuation due to losses (either material or radiation losses). Taking advantage of this definition, it has been shown that the condition for maximixing directivity at broadside occurs in a region where reactive effects may be comparable to radiative effects.

In order to fully understand what kind of radiating performance one can expect for structures operating below (but close to) the cutoff frequency, we have also studied the wave impedance of leaky modes propagating in lossy parallel-plate waveguides. It turned out that, at the frequency for which directivity at broadside is maximized the wave impedance is slightly more resistive rather than reactive (meaning that impedance matching is still practical), provided that the feed is electrically small. Nevertheless, we have shown through full-wave simulations that even in the case of quasi-resonant feeds, for which a poor matching would be expected, it is possible to design an hoc impedance matching network to have the antenna efficiently radiating below cutoff.

All theoretical results and analytical formulas have been validated through various numerical examples considering different models. Full-wave results have been provided for the relevant case study of a graphene planar waveguide operating in the terahertz range to show the consistency and accuracy of the proposed formulas in a realistic scenario.

Acknowledgment

The authors would like to thank the anonymous reviewer of [18] for having inspired this work thanks to their comments.

References

[1] N. Marcuvitz, "On field representations in terms of leaky modes or eigenmodes," *IRE Trans. Antennas Propag.*, vol. 4, no. 3, pp. 192–194, 1956.

[2] T. Rozzi and M. Mongiardo, *Open Electromagnetic Waveguides*. IEE Electromagnetic Waves Series, 1997, vol. 43.

[3] D. R. Jackson, C. Caloz, and T. Itoh, "Leaky-wave antennas," *Proceedings of the IEEE*, vol. 100, no. 7, pp. 2194–2206, 2012.

[4] F. Monticone and A. Alù, "Leaky-wave theory, techniques, and applications: from microwaves to visible frequencies," *Proc. IEEE*, vol. 103, no. 5, pp. 793–821, May 2015.

[5] N. K. Das, "Power leakage, characteristic impedance, and leakage-transition behavior of finite-length stub sections of leaky printed transmission lines," *IEEE Trans. Microw. Theory Tech.*, vol. 44, no. 4, pp. 526–536, 1996.

[6] ——, "A new theory of the characteristic impedance of general printed transmission lines applicable when power leakage exists," *IEEE Trans. Microw. Theory Tech.*, vol. 48, no. 7, pp. 1108–1117, 2000.

[7] P. Burghignoli, C. Di Nallo, F. Frezza, A. Galli, and P. Lampariello, "Efficient description of impedance and radiation features in printed-circuit leaky-wave structures–an unconventional scattering-matrix approach," *IEEE Trans. Microw. Theory Tech.*, vol. 48, no. 10, pp. 1661–1672, 2000.

[8] Y.-D. Lin and J.-W. Sheen, "Mode distinction and radiation-efficiency analysis of planar leaky-wave line source," *IEEE Trans. Microw. Theory Tech.*, vol. 45, no. 10, pp. 1672–1680, 1997.

[9] X.-Y. Zeng, S.-J. Xu, K. Wu, and K.-M. Luk, "Properties of guided modes on open structures near the cutoff region using a new version of complex effective dielectric constant," *IEEE Trans. Microw. Theory Tech.*, vol. 50, no. 5, pp. 1417–1424, 2002.

[10] T.-L. Chen, Y.-D. Lin, and J.-W. Sheen, "Microstrip-fed microstrip second higher order leaky-mode antenna," *IEEE Trans. Antennas Propag.*, vol. 49, no. 6, pp. 855–857, 2001.

[11] K. Y. Kim, H.-S. Tae, and J.-H. Lee, "Analysis of leaky modes in circular dielectric rod waveguides," *Electronics Lett.*, vol. 39, no. 1, pp. 61–62, 2003.

[12] S. Yang and J.-M. Song, "Analysis of guided and leaky TM_{0n} and TE_{0n} modes in circular dielectric waveguide," *Prog. Electromagn. Res. B*, vol. 66, pp. 143–156, 2016.

[13] K. Y. Kim, "Leaky mode dispersions of Goubau lines," *Microw. Opt. Technol. Lett.*, vol. 50, no. 2, pp. 523–525, 2008.

[14] J. Liu, Y. Li, and Y. Long, "Fundamental even leaky mode in microstrip line loaded with shorting vias," *IET Microw. Antennas Propag.*, vol. 11, no. 1, pp. 129–135, 2017.

[15] G. Lovat, P. Burghignoli, and D. R. Jackson, "Fundamental properties and optimization of broadside radiation from uniform leaky-wave antennas," *IEEE Trans. Antennas Propag.*, vol. 54, no. 5, pp. 1442–1452, May 2006.

[16] A. Sutinjo, M. Okoniewski, and R. H. Johnston, "Beam-splitting condition in a broadside symmetric leaky-wave antenna of finite length," *IEEE Antennas Wireless Propag. Lett.*, vol. 7, pp. 609–612, 2008.

[17] W. Fuscaldo, D. R. Jackson, and A. Galli, "General formulas for the beam properties of 1-D bidirectional leaky-wave antennas," *IEEE Trans. Antennas Propag.*, vol. 67, no. 6, pp. 3597–3608, Jun. 2019.

[18] W. Fuscaldo, "Rigorous evaluation of losses in uniform leaky-wave antennas," *IEEE Trans. Antennas Propag.*, vol. 68, no. 2, pp. 643–655, Feb. 2020.

[19] D. M. Pozar, *Microwave Engineering*. Hoboken, NJ, USA: John Wiley & Sons, 2009.

[20] O. Luukkonen, C. Simovski, G. Granet, G. Goussetis, D. Lioubtchenko, A. V. Raisanen, and S. A. Tretyakov, "Simple and accurate analytical model of planar grids and high-impedance surfaces comprising metal strips or patches," *IEEE Trans. Antennas Propag.*, vol. 56, no. 6, pp. 1624–1632, Jun. 2008.

[21] S. Tretyakov, *Analytical Modeling in Applied Electromagnetics*. Norwood, MA, USA: Artech House, 2003.

[22] W. Fuscaldo, S. Tofani, D. C. Zografopoulos, P. Baccarelli, P. Burghignoli, R. Beccherelli, and A. Galli, "Systematic design of THz leaky-wave antennas based on homogenized metasurfaces," *IEEE Trans. Antennas Propag.*, vol. 66, no. 3, pp. 1169–1178, Mar. 2018.

[23] T. Zhao, D. R. Jackson, J. T. Williams, and A. Oliner, "Simple CAD model for a dielectric leaky-wave antenna," *IEEE Antennas Wireless Propag. Lett.*, vol. 3, no. 1, pp. 243–245, 2004.

[24] R. Sorrentino, "Transverse resonance technique," in *Numerical Techniques for Microwave and Millimeter-Wave Passive Structures*, T. Itoh, Ed. New York, NY, USA: John Wiley & Sons, 1989, ch. 11.

[25] V. Galdi and I. M. Pinto, "A simple algorithm for accurate location of leaky-wave poles for grounded inhomogeneous dielectric slabs," *Microw. and Opt. Technol. Lett.*, vol. 24, no. 2, pp. 135–140, 2000.

[26] D. R. Jackson, P. Burghignoli, G. Lovat, F. Capolino, J. Chen, D. R. Wilton, and A. A. Oliner, "The fundamental physics of directive beaming at microwave and optical frequencies and the role of leaky waves," *Proceedings of the IEEE*, vol. 99, no. 10, pp. 1780–1805, 2011.

[27] "VDI Virginia Diodes, Inc., Waveguide band designations." [Online]. Available: http://vadiodes.com/VDI/pdf/waveguidechart200908.pdf

[28] W. Fuscaldo, P. Burghignoli, P. Baccarelli, and A. Galli, "Graphene Fabry-Perot cavity leaky-wave antennas: Plasmonic versus nonplasmonic solutions," *IEEE Trans. Antennas Propag.*, vol. 65, no. 4, pp. 1651–1660, Apr. 2017.

[29] F. D'Angelo, Z. Mics, M. Bonn, and D. Turchinovich, "Ultra-broadband THz time-domain spectroscopy of common polymers using THz air photonics," *Opt. Express*, vol. 22, no. 10, pp. 12 475–12 485, 2014.

[30] A. Ip and D. R. Jackson, "Radiation from cylindrical leaky waves," *IEEE Trans. Antennas Propag.*, vol. 38, no. 4, pp. 482–488, Apr. 1990.

[31] R. F. Harrington, *Time-Harmonic Electromagnetic Fields*. New York, NY, USA: IEEE Press, 2015.

[32] F. Scattone, M. Ettorre, B. Fuchs, R. Sauleau, and N. J. Fonseca, "Synthesis procedure for thinned leaky-wave-based arrays with reduced number of elements," *IEEE Trans. Antennas Propag.*, vol. 64, no. 2, pp. 582–590, 2015.

[33] F. Scattone, M. Ettorre, R. Sauleau, N. T. Nguyen, and N. J. Fonseca, "Optimization procedure for planar leaky-wave antennas with flat-topped radiation patterns," *IEEE Trans. Antennas Propag.*, vol. 63, no. 12, pp. 5854–5859, 2015.

[34] N. Llombart, A. Neto, G. Gerini, M. Bonnedal, and P. De Maagt, "Impact of mutual coupling in leaky wave enhanced imaging arrays," *IEEE Trans. Antennas Propag.*, vol. 56, no. 4, pp. 1201–1206, 2008.

[35] D. Blanco, N. Llombart, and E. Rajo-Iglesias, "On the use of leaky wave phased arrays for the reduction of the grating lobe level," *IEEE Trans. Antennas Propag.*, vol. 62, no. 4, pp. 1789–1795, 2013.

[36] M. A. Hickey, M. Qiu, and G. V. Eleftheriades, "A reduced surface-wave twin arc-slot antenna for millimeter-wave applications," *IEEE Microw. Wireless Comp. Lett.*, vol. 11, no. 11, pp. 459–461, 2001.

[37] N. Marcuvitz, *Waveguide Handbook*. London, UK: IEE, 1951, no. 21.

[38] "CST products Darmstadt, Germany, 2019." [Online]. Available: http://www.cst.com

[39] H. W. Bode, *Network Analysis and Feedback Amplifier Design*. New York, NY, USA: Van Nostrand, 1945.

[40] R. M. Fano, "Theoretical limitations on the broadband matching of arbitrary impedances," *J. Franklin Inst.*, vol. 249, no. 1, pp. 57–83, 1950.

[41] A. Ferraro, D. C. Zografopoulos, R. Caputo, and R. Beccherelli, "Broad-and narrow-line terahertz filtering in frequency-selective surfaces patterned on thin low-loss polymer substrates," *IEEE J. Sel. Topics Quantum Electron.*, vol. 23, no. 4, pp. 1–8, 2017.

[42] G. W. Hanson, "Dyadic Green's functions and guided surface waves for a surface conductivity model of graphene," *J. Appl. Phys.*, vol. 103, no. 6, p. 064302, 2008.

[43] W. Fuscaldo, P. Burghignoli, P. Baccarelli, and A. Galli, "Complex mode spectra of graphene-based planar structures for THz applications," *J. Infrared Milli. Terahz Waves*, vol. 36, no. 8, pp. 720–733, Aug. 2015.

[44] ——, "Efficient 2-D leaky-wave antenna configurations based on graphene metasurfaces," *Int. J. Microwave Wireless Techn.*, vol. 9, no. 6, pp. 1293–1303, 2017.

[45] G. Lovat, G. W. Hanson, R. Araneo, and P. Burghignoli, "Semiclassical spatially dispersive intraband conductivity tensor and quantum capacitance of graphene," *Phys. Rev. B*, vol. 87, no. 11, p. 115429, 2013.

[46] C. L. Holloway, A. Dienstfrey, E. F. Kuester, J. F. OHara, A. K. Azad, and A. J. Taylor, "A discussion on the interpretation and characterization of metafilms/metasurfaces: The two-dimensional equivalent of metamaterials," *Metamaterials*, vol. 3, no. 2, pp. 100–112, 2009.

[47] T. Tamir and A. A. Oliner, "Guided complex waves. Part 1: fields at an interface," *Proc. IEE*, vol. 110, no. 2, pp. 310–324, Feb. 1963.

[48] ——, "Guided complex waves. Part 2: relation to radiation patterns," *Proc. IEE*, vol. 110, no. 2, pp. 325–334, Feb. 1963.

[49] D. R. Jackson and A. A. Oliner, "Leaky-Wave Antennas," in *Modern Antenna Handbook*, C. A. Balanis, Ed. New York, NY, USA: John Wiley & Sons, 2011, ch. 7.

[50] A. A. Oliner and D. R. Jackson, "Leaky-Wave Antennas," in *Antenna Engineering Handbook*, J. L. Volakis, Ed. New York, NY, USA: McGraw-Hill, 2007, ch. 11.

[51] A. A. Oliner, "Leaky-Wave Antennas," in *Antenna Engineering Handbook*, R. C. Johnson, Ed. New York, NY, USA: McGraw-Hill, 1984, ch. 10.

[52] Y.-W. Hsu, H.-C. Lin, and Y.-C. Lin, "Modeling and PCB implementation of standing leaky-wave antennas incorporating edge reflection for broadside radiation enhancement," *IEEE Trans. Antennas Propag.*, vol. 64, no. 2, pp. 461–468, 2015.

[53] V. R. Komanduri, D. R. Jackson, and S. A. Long, "Radiation characteristics of finite-length 1D-uniform leaky wave antennas radiating at broadside," in *2010 Int. Symp. Antennas Propag., Toronto, USA*. IEEE, 2010.

[54] P. Burghignoli, D. Comite, W. Fuscaldo, P. Baccarelli, and A. Galli, "Higher-order cylindrical leaky waves–Part II: Circular array design and validations," *IEEE Trans. Antennas Propag.*, vol. 67, no. 11, pp. 6748–6760, 2019.

[55] G. N. Watson, *A Treatise on the Theory of Bessel Functions*. Cambridge, UK: Cambridge University Press, 1995.

[56] M. Abramowitz and I. A. Stegun, *Handbook of Mathematical Functions*. New York, NY, USA: Dover, 1962.